Improved Crystalline Structure and Enhanced Photoluminescence of ZnO Nanolayers in Bi2Se3/ZnO Heterostructures

Margarita Baitimirova, Jana Andzane, Roman Viter, Bernard Fraisse, Octavio Graniel, Mikhael Bechelany, John Watt, Domantas Peckus, Sigitas Tamulevicius, Donats Erts

Improved Crystalline Structure and Enhanced Photoluminescence of ZnO Nanolayers in Bi_2Se_3/ZnO Heterostructures

*Margarita Baitimirova[1], Jana Andzane[1], Roman Viter[2], Bernard Fraisse[4], Octavio Graniel[5], Mikhael Bechelany[5], John D. Watt,[6] Domantas Peckus[7], Sigitas Tamulevicius[7], Donats Erts[1,3]**

[1]Institute of Chemical Physics, [2]Institute of Atomic Physics and Spectroscopy, and [3]Department of Chemistry, University of Latvia, Raina Boulevard 19, LV 1586, Riga, Latvia

[4]Institute Charles Gerhardt, University of Montpellier, UMR 5253 CNRS-UM-ENSCM, Place Eugene Bataillon, 34095, Montpellier, France

[5]European Institute of Membranes, University of Montpellier, CNRS, ENSCM, Place Eugene Bataillon, 34095 Montpellier, France

[6]Center for Integrated Nanotechnologies, Los Alamos National Laboratory, Albuquerque, NM 87185-1315, US

[7]Institute of Materials Science, Kaunas University of Technology, K. Barsausko st. 59, LT-51423, Kaunas, Lithuania

*E-mail: donats.erts@lu.lv

KEYWORDS: zinc oxide, bismuth selenide, photoluminescence, interface, nanostructures

ABSTRACT

Bi_2Se_3/ZnO heterostructure is a new combination of high and low band gap nanomaterials that can be implemented for optoelectronic devices. Influence of the Bi_2Se_3 substrate on crystallization of ZnO nanolayers and charge separation at the Bi_2Se_3/ZnO interface are important parameters, which affect optical and electronic properties of the heterostructure. Despite a few works on Bi_2Se_3/ZnO heterostructures, the mechanisms of enhanced optical properties and correlation between optical and structural properties in such heterostructures are not studied in detail. In the present paper, we report on structure and optical properties of ZnO nanolayers with different thicknesses (10-150 nm) deposited by atomic layer deposition on planar and non-planar Bi_2Se_3 nanostructured coatings. Crystallization of ZnO nanolayers grown on Bi_2Se_3 and Si substrates was analyzed by X-ray diffraction, Scanning and Transmission Electron Microscopy methods. Enhancement of ZnO photoluminescence in Bi_2Se_3/ZnO heterostructures in comparison to the photoluminescence of the same thickness ZnO nanolayers deposited on p-doped Si substrates was observed. Correlation between the structure and optical properties of ZnO nanolayers in Bi_2Se_3/ZnO heterostructures is analyzed. Three complementary mechanisms of enhancement of optical properties of ZnO in Bi_2Se_3/ZnO heterostructures, based on charge separation at the Bi_2Se_3/ZnO interface, improvement of ZnO crystalline structure and surface plasmon-photon coupling are proposed.

INTRODUCTION

Zinc oxide (ZnO) is known as n-type semiconductor with good transparency and strong luminescence at room temperature.[1] The high photosensitivity, chemical stability and non-toxicity make it to be a promising material for applications in light emitting diodes (LEDs),[2,3] UV,[4–9] gas[10] and biosensors.[11,12]

Among different methods of fabrication, atomic layer deposition (ALD) provides homogenous and conformal coating of ZnO on substrates with different shape and surface roughness.[13–15] Structure and optical properties of ZnO depend on type of substrate, temperature of deposition and thickness of the deposited layers.[14–16] It was shown that transition from amorphous to crystalline structure in ZnO layers was observed with increasing of the layer thickness beyond 50 nm.[14] Improvement of ZnO crystalline structure in the layers with thicknesses below 50 nm was demonstrated in Al_2O_3/ZnO and graphene/ZnO nanolaminates, where ZnO layers were deposited on Al_2O_3 and graphene layers, respectively.[15–18] In addition to improvement of the crystalline structure, the optical properties of ZnO in the nanolaminate structures were found to be dependent also on charge transfer on the interface between ZnO and Al_2O_3, and between ZnO and graphene.[15–18] Modelling of Al_2O_3/ZnO heterostructures confirmed that the combination of ZnO (band gap ~3.3 eV) with a material with larger band gap as Al_2O_3 (band gap ~ 6eV) results in increase of the photoluminescence (PL) of ZnO in Al_2O_3/ZnO heterostructure due to the charge transfer at the interfaces and decrease of the surface potential in ZnO upper layers.[16] On the other hand, forming of heterostructures of ZnO and nanomaterials with the lower in comparison with ZnO band gap is advantageous for optoelectronic applications related to photoactive charge separation in visible and NIR range.

Combination of nanolayers of ZnO and narrow band gap semiconductors as Bi_2Se_3, Bi_2Te_3 or Bi_2S_3 in heterostructures is a novel approach that can be implemented for optoelectronic devices and other applications. For instance, Bi_2S_3/ZnO heterostructures were recently demonstrated as an excellent photocatalyst for visible-light-driven hydrogen generation and a highly efficient photocatalyst for dye degradation under visible light irradiation.[19]

Bismuth selenide (Bi_2Se_3) is a narrow band gap semiconductor, which belongs to a class of topological insulators with surface states protected from scattering by time reversal symmetry.[20] The presence of the

surface states in Bi_2Se_3 have been experimentally identified by reducing the bulk conductance using different approaches as tuning the gate voltage, introducing dopants and nanostructuring.[21–23]

Some previous research on optical, electronic properties of ZnO/Bi_2Te_3 hybrid structures prepared by mechanical placement of exfoliated Bi_2Te_3 flakes on the surface of ZnO crystal revealed enhancement of the PL of ZnO, which has been attributed to the surface plasmon resonance.[24] It has been reported also that deposition of ZnO as protection nanolayer on top of Bi_2Se_3 nanostructures results in decrease of the free electron concentration in Bi_2Se_3.[25] However, the mechanisms of enhanced optical properties and correlation between optical and structural properties in such heterostructures have not been studied in detail.

In this study, Bi_2Se_3/ZnO heterostructures were fabricated by ALD deposition of 10-150 nm thin ZnO nanolayers on top of Bi_2Se_3 nanostructured coatings grown on graphene (further in text G/Bi_2Se_3/ZnO heterostructures) and quartz (further in text Q/Bi_2Se_3/ZnO heterostructures) by catalyst-free vapor-solid deposition.[21,26] Influence of Bi_2Se_3 morphology on structure and on optical properties of ZnO nanolayers was investigated. The obtained results were compared with the properties of ZnO nanolayers deposited by ALD on p-doped Si substrates (further in text Si/ZnO heterostructures). Band gap diagram of the Bi_2Se_3/ZnO interface and possible mechanisms of PL enhancement in the Bi_2Se_3/ZnO heterostructures are discussed.

EXPERIMENTAL METHODS

Q/Bi_2Se_3/ZnO and G/Bi_2Se_3/ZnO heterostructure preparation. Graphene substrates used for the experiments were synthesized by copper-catalysed low-pressure chemical vapour deposition (CVD reactor First Nano Easy tube 101), using methane, diluted in hydrogen, as a carbon source. The

synthesized graphene sheets were transferred onto quartz surface using polymer-assisted transfer technique, as reported elsewhere.[27,28]

Bi_2Se_3 nanostructured coatings of thicknesses ~110 – 130 nm were synthesized using catalyst-free vapour-solid deposition method in a horizontal tube of single-zone quartz tube furnace (GSL-1100X, MTI Corp.) on quartz and graphene substrates, as previously described elsewhere.[26,29,30] Bi_2Se_3 crystals (99.99% Sigma Aldrich) were used as a source material, which was evaporated at 585 °C temperature and deposited on substrates placed downstream at 330-380 °C temperature. The pressure inside the tube during the synthesis gradually increased from 200 mTorr to 4 Torr.

ZnO nanolayers of different thicknesses (from 10 nm to 150 nm) were synthesized onto prepared Bi_2Se_3 nanostructures as well as on p-doped Si substrates ((100), Si-Mat) by ALD method using a homemade reactor under the same conditions as described elsewhere.[31] Diethylzinc (95%, STREM Chemicals Inc.) was used as a zinc precursor and water – as an oxidant. ZnO growth rate was 0.2 nm/cycle at 100 °C temperature.

Characterisation. The morphology and chemical composition of synthesized Q/Bi_2Se_3/ZnO and G/Bi_2Se_3/ZnO heterostructures were characterized using a field emission scanning electron microscope (SEM) Hitachi S-4800 equipped with an energy dispersive X-ray (EDX) analyser B-QANTAX.

The crystalline structure of fabricated heterostructures was studied using X-ray diffraction spectroscopy (XRD) by powder diffractometer X'PERT MRD with Cu Kα radiation and high-resolution transmission electron microscopy (HRTEM). For HRTEM characterization, an electron transparent cross-section lamella was prepared by focused ion beam (FIB) milling and lift-out in a Thermo Fisher Scientific Scios 2 Dual Beam SEM/FIB. The FIB lamella was attached to a Cu half grid and further thinned by low keV milling using the Ga+ beam. HRTEM was performed on a FEI Titan environmental TEM with Image Cs corrector operating at 300 keV. Elemental analysis was carried out using a FEI

Tecnai G2 F30 TEM equipped with an EDAX X-ray energy dispersive spectroscopy (XEDS) detector. Fast Fourier Transform (FFT) of the selected areas of the HRTEM images was performed using ImageJ software.

Optical properties of Q/Bi_2Se_3/ZnO and G/Bi_2Se_3/ZnO heterostructures were studied with UV-Vis transmittance (fiber optics spectrometer Ocean Optics HR2000+), reflectance and PL spectroscopy in a wavelength range 340 - 775 nm. The excitation of luminescence was performed by a nitrogen laser source 266 nm wavelength (output 30 mW/cm^2). The obtained PL spectra were deconvoluted using MagicPlot 2.7.1.0 software by splitting the spectra in separate peaks with the Gaussian fitting, keeping maxima positions of all subpeaks fixed within ±0.02 eV and full width at half maximum (FWHM) within ±0.03 eV. The integrated PL intensity was calculated from the values obtained after deconvolution by the multiplying the intensity of subpeak by its half width at half maximum (HWHM).

RESULTS AND DISCUSSION

Morphology. SEM images of G/Bi_2Se_3 and Q/Bi_2Se_3 nanostructured substrates covered with ZnO nanolayers show that the Bi_2Se_3 coatings deposited on graphene surface consist from coalesced horizontally oriented nanoplates with rare inclusion of the nanoplates oriented under an angle relative to the substrate (Figure 1a). In contrast, in the Bi_2Se_3 coatings deposited on quartz a significant number of randomly oriented nanoplates was observed (Figure 1b). The EDX mapping showed that the ALD-deposited ZnO nanolayers uniformly covered the surface of Bi_2Se_3 (Figure 1c).

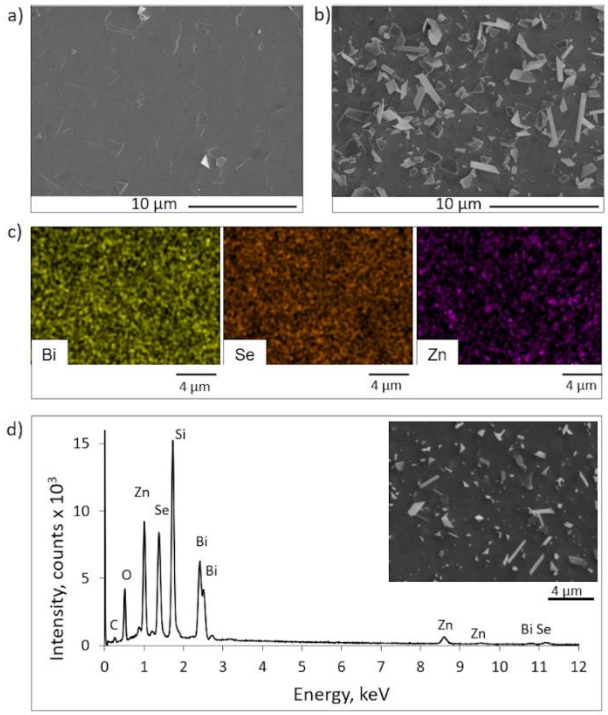

Figure 1. SEM images of ~110-130 nm thin Bi_2Se_3 nanostructures covered with 50 nm thin ZnO nanolayer: a) G/Bi_2Se_3/ZnO heterostructure, b) Q/Bi_2Se_3/ZnO heterostructure, c) an example of SEM-EDX mapping, and d) EDX spectrum of fabricated Q/Bi_2Se_3/ZnO heterostructure.

The EDX measurements performed after the ZnO deposition (Figure 1d) showed that Bi and Se content in the fabricated G/Bi_2Se_3/ZnO and Q/Bi_2Se_3/ZnO heterostructures is respectively (39±3) at% and (61±3) at%, which within the measurement accuracy corresponds to the stoichiometric Bi_2Se_3 compound. This confirms non-destructive nature of low-temperature (100 °C) ALD ZnO deposition on already fabricated Bi_2Se_3 nanostructures.

The XRD spectra of G/Bi_2Se_3/ZnO and Q/Bi_2Se_3/ZnO heterostructures revealed the crystalline nature of the deposited 10-100 nm thin ZnO nanolayers and underlying Bi_2Se_3 (Figure 2). No reflections other than Bi_2Se_3 compounds (for example Bi_4Se_3, Bi_3Se_4) or by-products that may form during ZnO ALD process on Bi_2Se_3 (for example, ZnSe)[32] were detected.

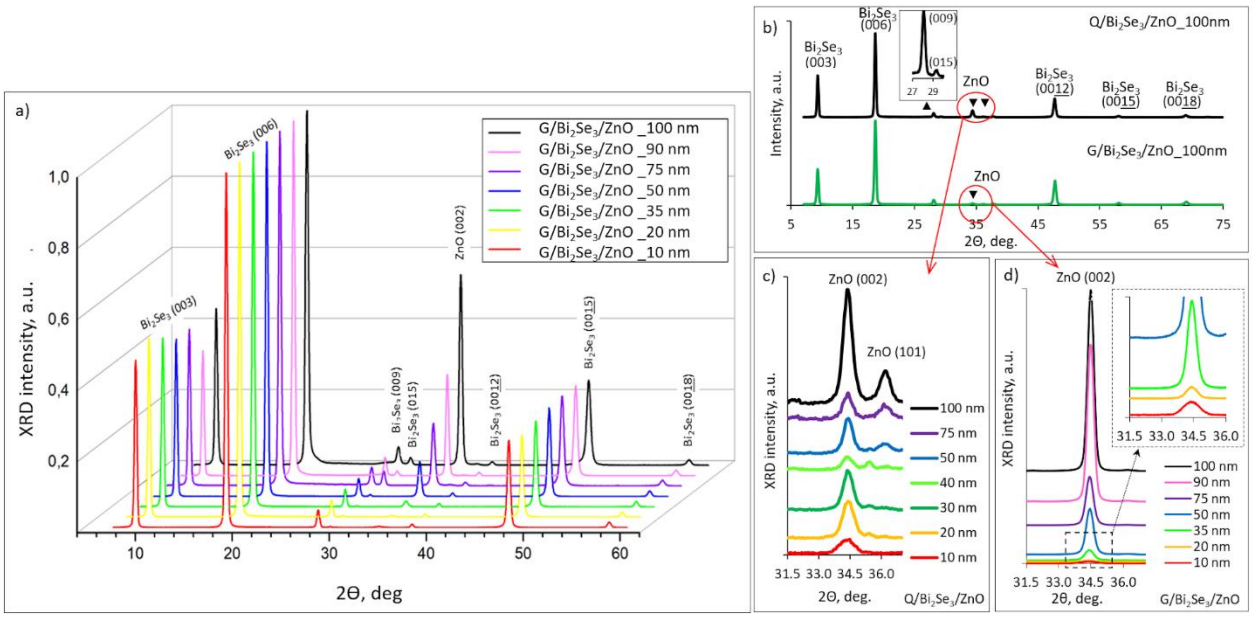

Figure 2. Full XRD spectra of a) G/Bi_2Se_3/ZnO heterostructures with ZnO nanolayers thicknesses 10-100 nm; b) G/Bi_2Se_3/ZnO (green) and Q/Bi_2Se_3/ZnO (black) heterostructures with ZnO nanolayer thickness 100 nm; c,d) enlarged images of the region of ZnO diffraction plane positions for the Q/Bi_2Se_3/ZnO (c) and G/Bi_2Se_3/ZnO (d and d, inset) heterostructures with different ZnO nanolayers thicknesses.

The highly intensive diffraction peaks at 2Θ= 9.25°, 18.57°, 47.59° and low intensity peaks at 2Θ= 28.14°, 37.86° and 58.18° detected in XRD spectra of G/Bi_2Se_3/ZnO and Q/Bi_2Se_3/ZnO heterostructures (Figures 2a,b) correspond to (003), (006), (00$\underline{15}$), (009), (00$\underline{12}$) and (00$\underline{18}$) reflection planes of rhombohedral crystal lattice of Bi_2Se_3.[33] This indicates the [00*l*] growth direction of synthesized by catalyst-free vapour-solid deposition method Bi_2Se_3, with the crystallographic c-axis oriented perpendicularly to the substrate surface. XRD of Q/Bi_2Se_3/ZnO heterostructures revealed also low intensity peak at 2Θ= 29.36°, indicating (015) reflection plane of Bi_2Se_3 (Figure 2b black line, inset).

This diffraction peak can be attributed to the presented in the Q/Bi_2Se_3/ZnO heterostructures Bi_2Se_3 nanoplates oriented under different angles relative to the substrate surface (Figure 1b).[26]

The XRD spectra obtained for the fabricated G/Bi_2Se_3/ZnO and Q/Bi_2Se_3/ZnO heterostructures (Figures 2a,b) were used for the study of the absence or presence of characteristic for ZnO diffraction peaks and for the extraction of their FWHM values.

The ZnO lattice constant *c* and *d*-spacing between the atomic planes for ZnO nanolayers were calculated from the obtained XRD spectra of Q/Bi_2Se_3/ZnO and G/Bi_2Se_3/ZnO heterostructures, applying formula for hexagonal ZnO crystal lattice:[34]

$$\frac{1}{d^2} = \frac{4}{3} \cdot \left(\frac{h^2+kh+k^2}{a^2}\right) + \frac{l^2}{c^2} \quad (1)$$

where *d* is interplanar spacing; *h, k, l* are Miller indices; *a* and *c* are lattice constants.

The calculated values for ZnO lattice constant *c* and d-spacing were (0.521 ± 0.014) nm and (0.261 ± 0.005) nm respectively for ZnO nanolayers in both G/Bi_2Se_3/ZnO and Q/Bi_2Se_3/ZnO heterostructures. These values are consistent with the ZnO lattice parameters for 100 nm ALD thin film deposited on Si substrate ((c = 0.5213 nm and d = 0.2606 nm)[14].

Presence of characteristic for ZnO diffraction peaks already for 10 nm thick ZnO layers indicates highly crystalline structure of 10-100 nm thin ZnO nanolayers in G/Bi_2Se_3/ZnO and Q/Bi_2Se_3/ZnO heterostructures in comparison with Si/ZnO heterostructures, where the transition from amorphous (below 20 nm of thickness) and semi-amorphous (of thicknesses 20-50 nm) to crystalline state was observed for ZnO thicknesses starting from 50 nm.[31]

For all G/Bi_2Se_3/ZnO heterostructures, the only detected ZnO reflection peak corresponds to (002) plane (Figure 2d, peak at 2Θ=34.38°). This indicates one-direction growth of ZnO grains on G/Bi_2Se_3 substrate and differs significantly from the ALD growth of ZnO on Si, which results in formation of

polycrystalline thin films, showing two main diffractions peaks corresponding to (100) and (101) reflection planes.[31]

For the Q/Bi_2Se_3/ZnO heterostructures, the reflection peak of ZnO (002) plane was also dominating for all range of ZnO thicknesses, however, its intensity was lower in comparison with G/Bi_2Se_3/ZnO samples. One of two characteristic for polycrystalline ALD-deposited on Si substrates ZnO films diffraction peaks – the peak related to (101) reflection plane - was detected for Q/Bi_2Se_3/ZnO samples with ZnO thicknesses starting from 50 nm (Figure 2c). Therefore, in contrast with the G/Bi_2Se_3/ZnO heterostructures, promoting one-direction growth of ZnO grains, the Q/Bi_2Se_3 substrates promote also growth of ZnO grains in one of directions, characteristic also for Si/ZnO thin films, starting from the ZnO nanolayers thicknesses of 50 nm. However, the absence of the main for Si/ZnO thin films (100) diffraction peak in Q/Bi_2Se_3/ZnO XRD spectra indicates ZnO growth mechanism like G/Bi_2Se_3/ZnO heterostructures. The lower in comparison with G/Bi_2Se_3/ZnO heterostructures intensities of the ZnO (002) reflection peak and the presence of the (101) reflection peak may be explained by the morphology of the Q/Bi_2Se_3 substrate surface, promoting growth of the ZnO nanolayers not only parallel to the quartz surface, but also under different directions relative to it (on surfaces of the randomly oriented Bi_2Se_3 nanoplates).

Figure 3a confirms the orientation of ZnO crystalline grains in different directions in the Q/Bi_2Se_3/ZnO heterostructure with ZnO nanolayer thickness 50 nm.

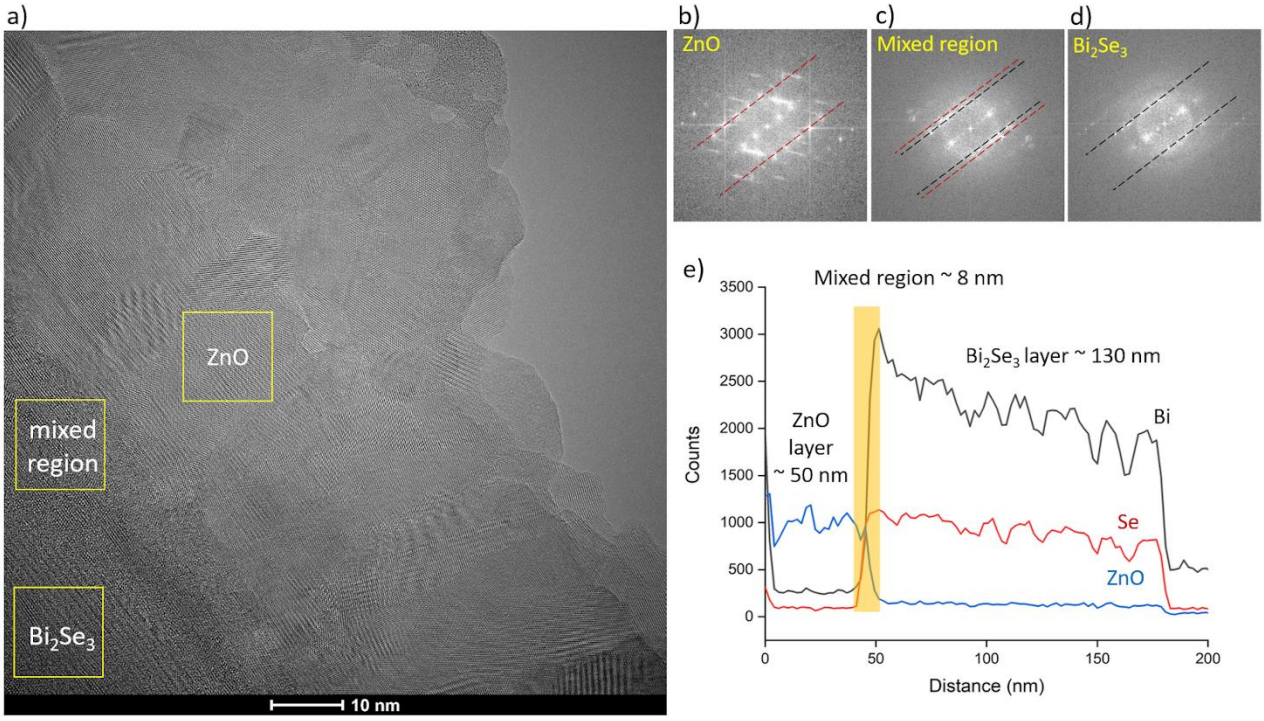

Figure 3. a) HRTEM image of the crossection of Q/Bi_2Se_3/ZnO heterostructure with ZnO nanolayer thickness 50 nm; b-d) FFT images of ZnO, mixed region at the Bi_2Se_3/ZnO interface and Bi_2Se_3, taken from the areas of the sample labelled with squares at the HRTEM image; e) Line EDX scan of the crossection of the Q/Bi_2Se_3/ZnO (50 nm) sample.

FFT and XEDS analysis performed for the crossection of Q/Bi_2Se_3/ZnO heterostructure (Figures 3b-e) revealed the presence of approximately 8 nm thin transition layer at the Bi_2Se_3/ZnO interface. Beyond this thickness, the ZnO nanolayer was found to be consisting of crystalline grains (Figure 3a).

The apparent crystalline grain sizes were estimated from the ZnO (002) diffraction peaks of the XRD spectra of G/Bi_2Se_3/ZnO and Q/Bi_2Se_3/ZnO heterostructures using the Scherrer's equation[35]:

$$D = \frac{K \cdot \lambda}{\beta \cdot \cos(\Theta)} \quad (2)$$

where λ is the X-ray wavelength, β is the integral half width, Θ is the Bragg angle. K factor value in this study equals 0.9 for considering not spherical shapes of the ZnO crystalline grains confirmed by the HRTEM images (Figures 3a,4a).

The lattice strain ε in ZnO was calculated using the following formula:[35]

$$\varepsilon = \frac{\beta}{4\,tan(\Theta)} \quad (3)$$

For more accurate analysis of grain size and strain effects, the instrumental line broadening must be accounted. The instrumental corrected broadening was calculated as follows:[35]

$$\beta = [(\beta_{measured})^2 - (\beta_{instrumental})^2]^{1/2} \quad (4)$$

It should be noted that even accounting the instrumental broadening, the precision of the grain size determination may be ±10-15%. Thus, in what follows, the general tendencies of the changes in grain sizes, not calculation of the exact ZnO grain sizes, are considered. The apparent crystalline grain size and lattice strain values for ZnO nanolayers, estimated using Equations (2) - (4) respectively, are shown in Figure 4 b,c.

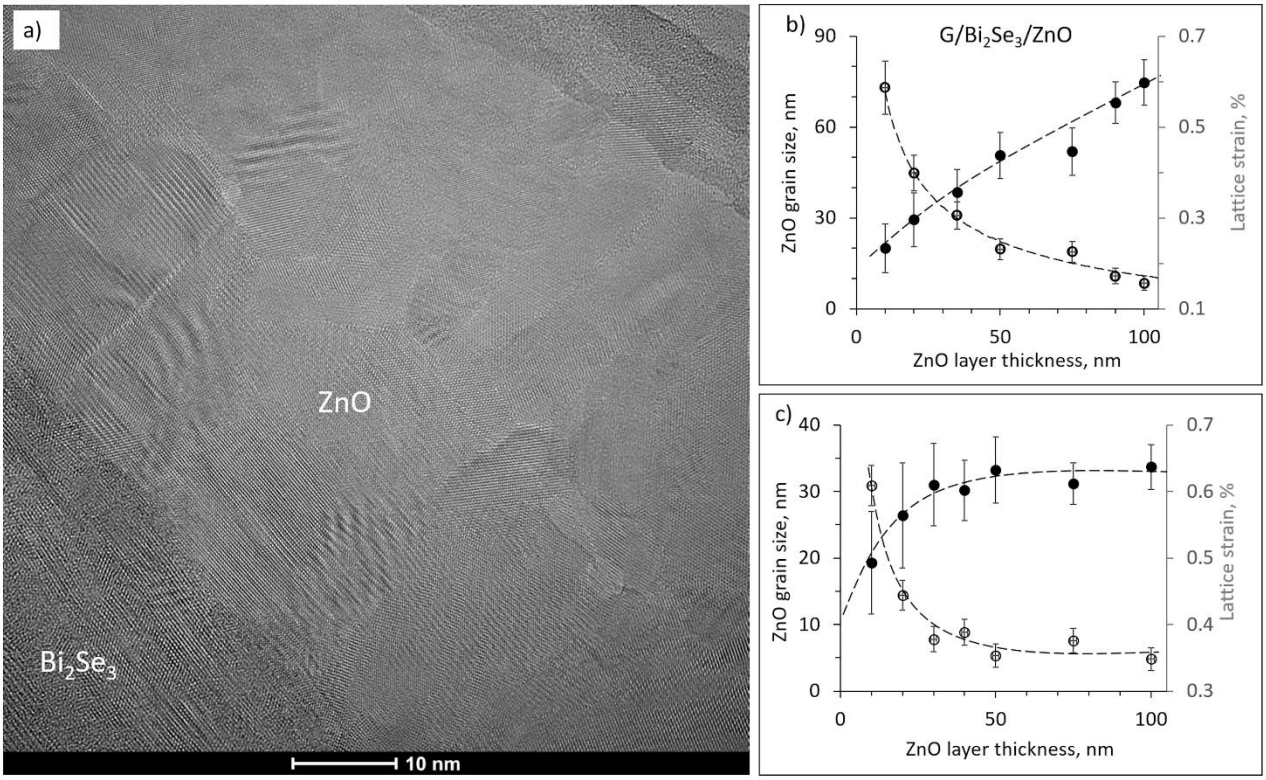

Figure 4. a) HRTEM image of the crossection of Q/Bi_2Se_3/ZnO heterostructure (thickness of ZnO nanolayer 50 nm); b-c) Apparent ZnO grain size (primary y-axis, black circles) and lattice strain (secondary y-axis, hollow circles) vs ZnO nanolayers thickness in b) G/Bi_2Se_3/ZnO, and c) Q/Bi_2Se_3/ZnO heterostructures.

G/Bi_2Se_3/ZnO heterostructures (Figure 4b) showed nearly linear tendency of increase of apparent grain size with the increase of ZnO nanolayer thickness, reaching values of approx. 75 nm for the 100 nm thin ZnO nanolayers, accompanied by simultaneous decrease of the lattice strain from 0.6% down to 0.15%. This indicates the improvement of the ZnO crystalline structure with the increase of ZnO nanolayer thickness. In contrast, for Q/Bi_2Se_3/ZnO heterostructures an increase in grain size, accompanied by a decrease in the lattice stress, was observed only for ZnO nanolayer thicknesses below 30 nm (Figure 4c). Above this value, the average ZnO grain size in the Q/Bi_2Se_3/ZnO heterostructures is approximately 30 nm and is practically unchanged, which is consistent with the sizes of grains visible at the HRTEM image

(Figure 4a). The smaller average size of the ZnO grains is probably related to the surface morphology of the Q/Bi_2Se_3 substrates, when ZnO growing on Bi_2Se_3 nanoplates of different orientations start to interfere with each other, thus hampering the formation of larger grains. Such difference between the grain sizes in G/Bi_2Se_3/ZnO and Q/Bi_2Se_3/ZnO heterostructures may lead to a higher number of formed at the ZnO grain boundaries optically active defects in Q/Bi_2Se_3/ZnO heterostructures in comparison with G/Bi_2Se_3/ZnO heterostructures.

Optical properties. Optical band gap (Eg) values for the ZnO nanolayers of G/Bi_2Se_3/ZnO and Q/Bi_2Se_3/ZnO heterostructures were estimated assuming a direct transition between valence and conduction bands and using the Tauc equation :[14]

$$ahv = B(hv - E_g)^r \quad (5)$$

where B is the constant, a is the absorption coefficient, hv is the incident photon energy, and r is the constant, which for direct transition equals ½.[36] E_g was graphically determined from the Tauc plots of $(ahv)^2$ vs hv (Figures 5a and 5b) by extrapolation the linear part of the absorption edge to ahv =0.

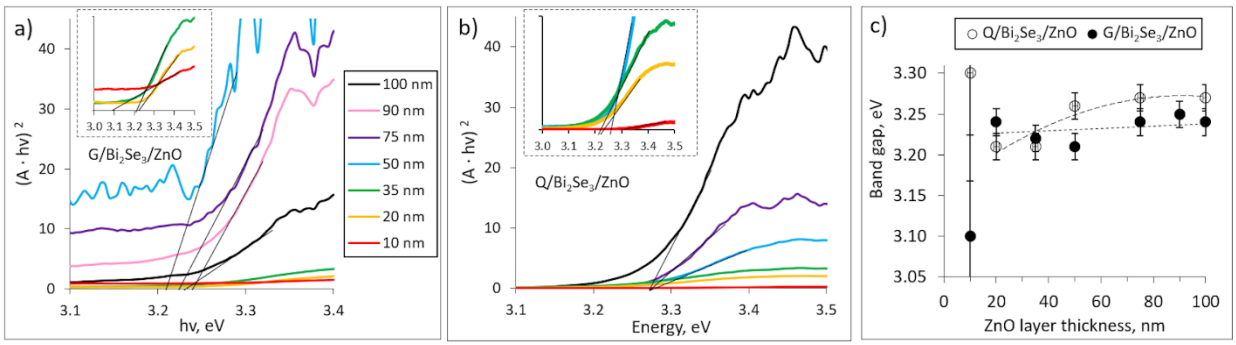

Figure 5. Band gap determination on the absorption edge from absorbance spectra for the ZnO nanolayers of different thicknesses in (a) G/Bi_2Se_3/ZnO and (b) Q/Bi_2Se_3/ZnO heterostructures; c) Band gap values vs ZnO nanolayer thickness in Q/Bi_2Se_3/ZnO and G/Bi_2Se_3/ZnO heterostructures.

The determined from the absorption spectra band gap values of ZnO nanolayers varied from 3.21 to 3.27 eV and from 3.21 to 3.25 eV for in Q/Bi_2Se_3/ZnO and G/Bi_2Se_3/ZnO heterostructures respectively (Figure 5 c). It should be noted that band gaps for 10 nm ZnO nanolayers are not taken into account in this data analysis as were determined with low accuracy. The weak absorption signal detected (insets of Figures 5a and 5b) may be related by the presence of the observed in HRTEM images 8 nm thin transition layer at the Bi_2Se_3/ZnO interface (Figure 3).

The obtained band gap values of ZnO in G/Bi_2Se_3/ZnO and Q/Bi_2Se_3/ZnO heterostructures were consistent with the optical band gap values reported previously for ZnO thin films on Si substrates (3.2 eV)[31,36] and are lower than typical band gap value of ZnO single crystal (3.37 eV).[37] Such optical band gap redshift of the ZnO nanolayers in Bi_2Se_3/ZnO heterostructures in comparison with the bulk ZnO may be related to higher (in comparison with single ZnO crystal) number of optically active point defects like Zn, O vacancies and Zn interstitials formed in the ZnO nanolayer near the Bi_2Se_3/ZnO interface, as well as at the ZnO grain boundaries. These defects may form shallow states in close to the conduction and valence bands of ZnO.[14,31,38–40] In this case, zone-to-centre transitions would result in reduction of the band gap value comparing to bulk ZnO.

Photoluminescence (PL) of the ZnO nanolayers in Q/Bi_2Se_3/ZnO and G/Bi_2Se_3/ZnO heterostructures was compared to the PL of the same thickness ALD ZnO thin films in Si/ZnO heterostructures. Generally, the PL spectra of all types of ZnO nanolayers exhibited two maxima (Figures 6 a-c): an intensive peak at ~3.2 eV and a broad peak centred at 2.3-2.4 eV.

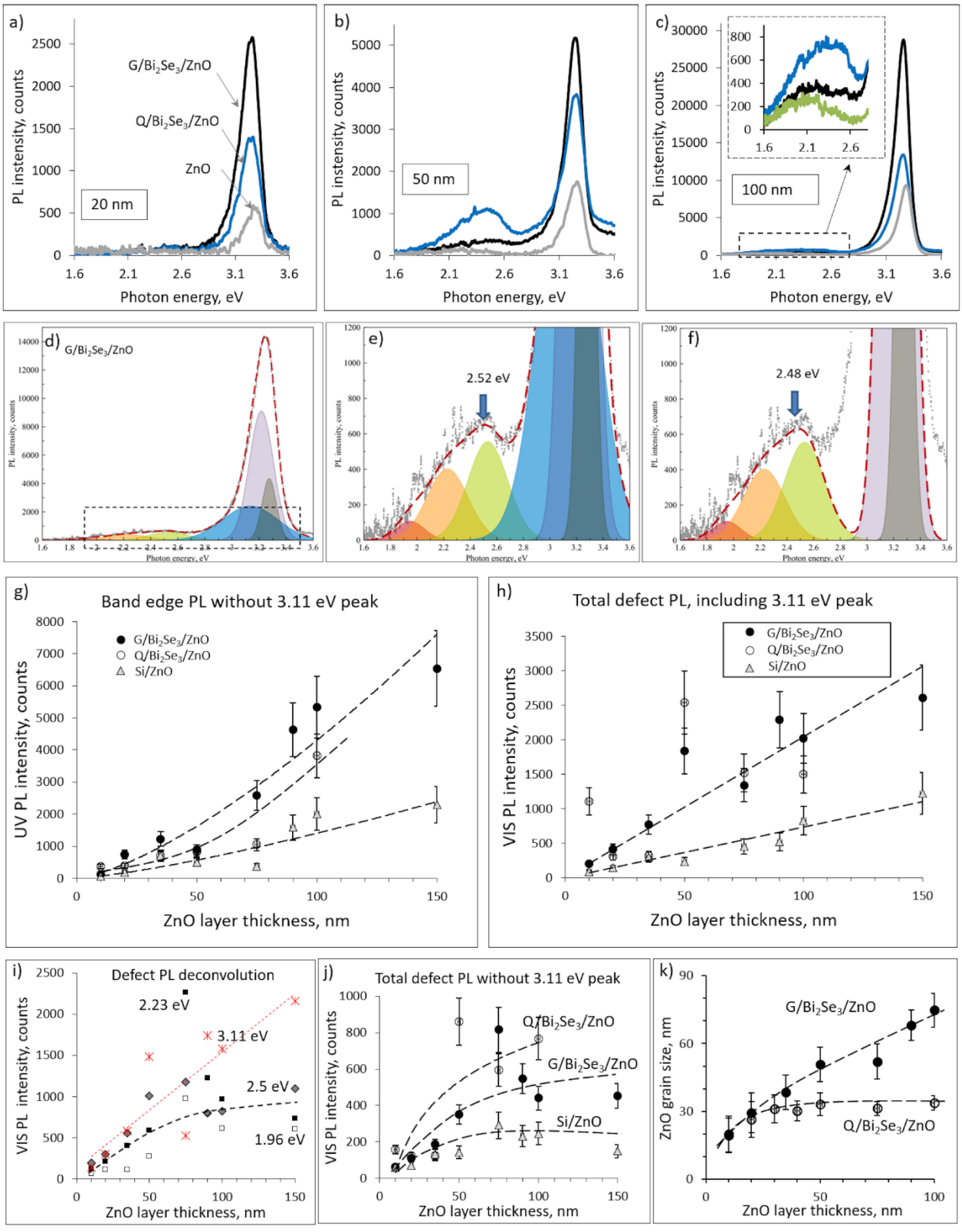
a)
PL instensity, counts
G/Bi2Se3/ZnO
Q/Bi2Se3/ZnO
ZnO
20 nm
Photon energy, eV
b)
PL instensity, counts
50 nm
Photon energy, eV
c)
PL instensity, counts
100 nm
Photon energy, eV
d)
G/Bi2Se3/ZnO
PL intensity, counts
Photon energy, eV
e)
2.52 eV
PL intensity, counts
Photon energy, eV
f)
2.48 eV
PL intensity, counts
Photon energy, eV
g)
Band edge PL without 3.11 eV peak
G/Bi2Se3/ZnO
Q/Bi2Se3/ZnO
Si/ZnO
UV PL intensity, counts
ZnO layer thickness, nm
h)
Total defect PL, including 3.11 eV peak
G/Bi2Se3/ZnO
Q/Bi2Se3/ZnO
Si/ZnO
VIS PL intensity, counts
ZnO layer thickness, nm
i)
Defect PL deconvolution
2.23 eV
3.11 eV
2.5 eV
1.96 eV
VIS PL intensity, counts
ZnO layer thickness, nm
j)
Total defect PL without 3.11 eV peak
Q/Bi2Se3/ZnO
G/Bi2Se3/ZnO
Si/ZnO
VIS PL intensity, counts
ZnO layer thickness, nm
k)
G/Bi2Se3/ZnO
Q/Bi2Se3/ZnO
ZnO grain size, nm
ZnO layer thickness, nm

Figure 6. Photoluminescence spectra of Q/Bi_2Se_3/ZnO, G/Bi_2Se_3/ZnO heterostructures and for the comparison - of ZnO thin films with different ZnO nanolayer thicknesses: a) 20 nm, b) 50 nm, c) 100 nm; d) an example of deconvoluted G/Bi_2Se_3/ZnO spectrum; e) deconvolution of the defect emission peak; f) deconvolution of the defect emission peak without the contribution of the defect peak related to the neutral Zn vacancies; g) band edge PL intensities of the G/Bi_2Se_3/ZnO, Q/Bi_2Se_3/ZnO and Si/ZnO vs ZnO nanolayer thickness; h) defect ZnO emission intensities of the G/Bi_2Se_3/ZnO, Q/Bi_2Se_3/ZnO and Si/ZnO vs ZnO nanolayer thickness (with the contribution of 3.11 eV peak related to the neutral Zn vacancies); i) intensities of emission peaks related to different types of defects thickness for G/Bi_2Se_3/ZnO heterostructures vs ZnO nanolayer thickness; j) defect ZnO emission intensities (without the contribution of 3.11 eV peak related to the neutral Zn vacancies) of the G/Bi_2Se_3/ZnO, Q/Bi_2Se_3/ZnO and Si/ZnO vs ZnO nanolayer thickness and k) comparison between the ZnO grain sizes in G/Bi_2Se_3/ZnO and Q/Bi_2Se_3/ZnO vs ZnO thickness.

Deconvolution of the photoluminescence spectra performed by Gaussian fitting (Figures 6d and 6e) revealed the presence of two PL peaks centered at 3.24 and 3.3 eV, which can be related to the ZnO band edge emission, and four PL peaks that can be related to the charge carrier recombination on different types of defects, such as neutral zinc interstitials (peak centred at ~ 3.11 eV), singly ionized oxygen and zinc vacancies (peak centred at ~ 2.5 eV), double ionized oxygen vacancies (peak centred at ~ 2.23 eV) and oxygen interstitials (peak centred at ~ 1.96 eV).[31,41,42]

As it can be seen from Figure 6e, the emission peak related to the neutral zinc interstitials (~3.11 eV) is significantly contributing to the total intensities of both maxima of the PL spectra. Traditionally, the influence of this peak is not separated from the summarized intensities of the band-edge and visible defect PL peaks of ZnO. In this work, the contribution of the defect emission peak centred at ~3.11 eV is removed from the total intensities of the band-edge and visible defect PL peaks as illustrated in Figure

6f in order to analyse the dynamics of the band-edge PL peaks centred at 3.24 eV and 3.3 eV, and the defect PL peaks centred at 1.96 eV, 2.23 eV and 2.5 eV.

Band-edge ZnO photoluminescence (3.24 eV, 3.3 eV). The intensity of the band-edge PL of ZnO in G/Bi_2Se_3/ZnO and Q/Bi_2Se_3/ZnO heterostructures for all ZnO nanolayer thicknesses was found to be significantly enhanced (by factor ~3.3 and ~1.7 respectively) in comparison with Si/ZnO heterostructures (Figure 6g). Enhancement of the band-edge PL of ZnO may be a result of superposition of several mechanisms: (i) charge transfer between the Bi_2Se_3 and ZnO nanolayers, (ii) improvement of crystalline structure of ZnO during the growth, and (iii) coupling of the band-edge excitons to surface-plasmon polaritons.

Charge transfer at the Bi_2Se_3/ZnO interface can be analysed within a band diagram (Figure 7a).

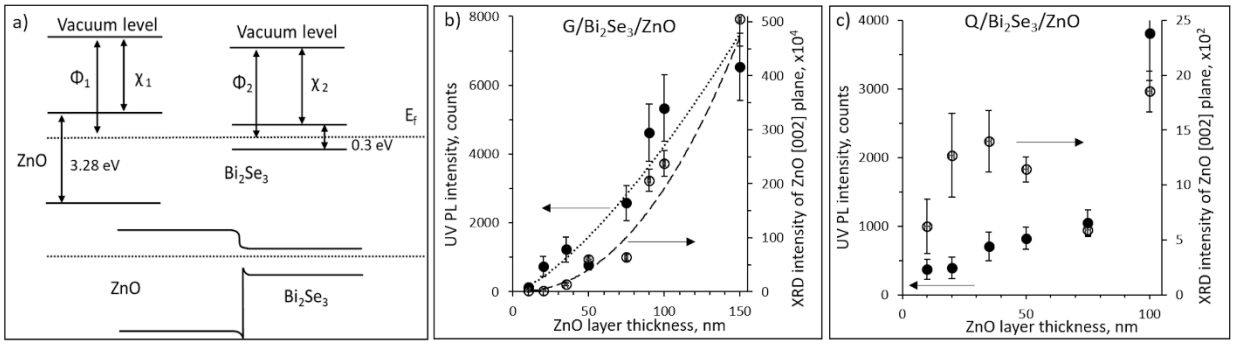

Figure 7. a) Band diagram for the Bi_2Se_3/ZnO interface. b,c) Dependence of ZnO PL intensity (primary y axis, black circles, dotted line) and XRD peak intensity (secondary y axis, hollow circles, dashed line) of G/Bi_2Se_3/ZnO (b) and Q/Bi_2Se_3/ZnO (c) heterostructures.

After forming a heterostructure, alignment of the Fermi level (E_f) in both contacting materials will occur. Position of the Fermi level E_F in each component of the heterostructure before joining them together was estimated as follows:[16]

$$E_F = \Phi - \chi, \quad (6)$$

where Φ is the work function and χ is the electron affinity.

The conductance band and valence band gap offsets were calculated as

$$\Delta E_c = \chi_2 - \chi_1 \quad (7)$$

$$\Delta E_v = \Delta E_g - \Delta E_c \quad (8)$$

where ΔE_g is the difference between the band gap values of ZnO and Bi_2Se_3, and χ_1 and χ_2 are the electron affinities of ZnO and Bi_2Se_3 respectively.

The built-in potential V_{bi} between the two altering ZnO and Bi_2Se_3 nanolayers was calculated as

$$V_{bi} \cdot q = E_{F1} - E_{F2} \quad (9)$$

where q is the electron charge, E_{F1} and E_{F2} are Fermi level positions in ZnO and Bi_2Se_3, correspondently.

Values of Bi_2Se_3 and ZnO parameters (work function, electron affinity and band gap), shown in Table 1 were taken from literature due to restriction of X-ray and ultraviolet photoelectron spectroscopy (XPS/UPS) methods for thick layers (over 20 nm).[16,43–45] The estimated by Equations (6)-(9) offsets of conductance band and valence ΔE_c, ΔE_v, and built in potential V_{bi}, between Bi_2Se_3 and ZnO are summarized in Table 1.

Table 1. Electronic parameters of ZnO and Bi_2Se_3.

	Φ, eV	X, eV	E_g, eV	ΔE_c, eV	ΔE_v, eV	V_{bi}, eV
ZnO[16]	5.8	4.35	3.28	0.95	2.03	1.35
Bi_2Se_3[43–46]	5.4	5.3	0.3			

In contrast with Si/ZnO deposited on p-doped Si substrates, where the depleted regions are formed near the interface in both Si and ZnO, the junction of ZnO and Bi_2Se_3 in a heterostructure results in formation of the electron-rich and hole-rich areas in ZnO and Bi_2Se_3, respectively. Forming of the hole-rich region in Bi_2Se_3 will result in decrease of electron concentration in this material.[25] Forming of the electron-rich area in ZnO will reduce the depletion layer formed at the surface of ZnO due to the

chemisorption of oxygen.[14,16,46] This depletion layer separates electrons and holes created by the above-bandgap illumination and restricts the exciton formation. Reduction of the depletion layer of ZnO due to formation of the Bi_2Se_3/ZnO heterojunction will lead to an increase of the band-edge PL of ZnO in comparison with the ZnO of the same thickness, deposited on p-doped Si substrates.

However, the equal for both G/Bi_2Se_3/ZnO and Q/Bi_2Se_3/ZnO heterostructures decrease of the ZnO depletion layer does not explain the significantly higher band-edge PL of the ZnO in G/Bi_2Se_3/ZnO heterostructures in comparison with the band-edge PL of the ZnO in Q/Bi_2Se_3/ZnO heterostructures (Figure 6g). This difference may be the result of other mechanisms of PL enhancement, discussed in the following paragraphs.

Figures 7b and 7c illustrate the correlation between the intensity of the XRD peak related to the ZnO (002) reflection plane and the intensity of the band-edge PL emission of ZnO in Bi_2Se_3/ZnO heterostructures.

The increase of the intensities of the XRD and the band-edge PL peaks with the increase of the ZnO thickness for the ZnO nanolayers in G/Bi_2Se_3/ZnO heterostructures (Figure 7a) is in line with the data related to the ZnO grain sizes (Figure 6k) and proves the role of improvement of the crystalline structure of the ZnO as one of the mechanisms for the band-edge PL enhancement. For the ZnO nanolayers in Q/Bi_2Se_3/ZnO heterostructures, the correlation between the values of intensities of XRD and band-edge PL is not convincing (Figure 7c), however, both PL and XRD intensities tend to increase at ZnO thickness above 75 nm. Presumably, in this case the ZnO crystallinity improvement is not the dominating mechanism for the band-edge PL enhancement. This conclusion is supported by the data shown in Figure 6k, demonstrating no increase of the ZnO grain size in Q/Bi_2Se_3/ZnO with the increase of the thickness of ZnO nanolayer.

However, the larger increase of the ZnO PL in the heterostructures in comparison with the increase of the intensity of the XRD peak (Figures 7b and 7c) may indicate the influence of the third mechanism of the PL enhancement, which is the coupling of the band-edge excitons to Bi_2Se_3 surface-plasmon polaritons similarly to the PL enhancement reported for the mechanically prepared ZnO/Bi_2Te_3 heterostructures.[24]

ZnO defect photoluminescence. The data on intensities of four peaks of ZnO defect emission related to different types of defects (neutral zinc interstitials (~3.11 eV), singly ionized oxygen and zinc vacancies (~2.5 eV), double ionized oxygen vacancies (~2.23 eV) and oxygen interstitials (~1.96 eV)) for G/Bi_2Se_3/ZnO, Q/Bi_2Se_3/ZnO and Si/ZnO are summarized in Figure 6 h. The defect PL of the ZnO nanolayers in G/Bi_2Se_3/ZnO heterostructures was 1.5-3 times higher in comparison with Si/ZnO heterostructures and showed linear increase with the ZnO nanolayer thickness. For the ZnO nanolayers in Q/Bi_2Se_3/ZnO heterostructures, the defect PL for different ZnO nanolayers thicknesses was up to 6 times higher in comparison with the defect PL of the Si/ZnO. The significantly higher defect PL of ZnO in Q/Bi_2Se_3/ZnO heterostructures in comparison with G/Bi_2Se_3/ZnO heterostructures may be explained by the smaller ZnO grain sizes resulting in larger area of grain boundaries in Q/Bi_2Se_3/ZnO heterostructures. The scatter of the intensity values in this case (Figure 6h, hollow circles) is presumably due to the deviations in the surface morphology of Q/Bi_2Se_3/ZnO samples.

Analysis of the defect emission peaks related to different types of defects for the G/Bi_2Se_3/ZnO heterostructures revealed that the linear enhancement of the summarized defect PL with the increase of the ZnO thickness (Figure 6h) is governed mostly by the defect peak related to the neutral zinc interstitials (~3.11 eV), which intensity increases linearly with the increase of ZnO nanolayer thickness (Figure 6 i). The intensities of other three peaks (~1.96 eV, ~2.23 eV and ~2.5 eV) of the defect emission of ZnO nanolayers increase with the increase of ZnO thickness from 10 to 75 nm, and then decrease/saturate for

the ZnO thicknesses above 75 nm (Figure 6j) in all samples. Also, it is seen from the Figure 6j that the defect PL of these emission peaks in G/Bi_2Se_3/ZnO and Q/Bi_2Se_3/ZnO samples is higher than PL of the Si/ZnO samples. Presumably, this enhancement of the defect ZnO PL in Bi_2Se_3/ZnO heterostructures is promoted by the decrease of the depletion layer in comparison to the ZnO films deposited on Si substrates.[14,31] Additionally, the increase of the defect emission intensity for the ZnO thicknesses below 75 nm may be related to the higher concentration of the single-ionized oxygen and zinc vacancies (~2.5 eV). As it is known, these defects are concentrated on the ZnO grain boundaries. As the ZnO grain size decreases with the decrease of the ZnO nanolayer thickness (Figure 6k), the thinner ZnO nanolayers may have higher concentration of defects. The dependence of the defect PL on ZnO grain size may explain also the higher defect PL of the ZnO in the Q/Bi_2Se_3/ZnO heterostructures in comparison with the G/Bi_2Se_3/ZnO (Figures 6j and 6k). The growth of the ZnO films above 75 nm is supported by the decrease of the defect concentration due to the increase of the grain size and the improvement of crystalline structure of the nanolayer,[31] which results in saturation of the defect PL.

CONCLUSIONS

Bi_2Se_3/ZnO heterostructures with different structure properties have been fabricated using consecutive physical vapor deposition and atomic layer deposition techniques. Improvement of the crystalline structure of ZnO nanolayers grown by ALD method on Q/Bi_2Se_3 and G/Bi_2Se_3 nanostructured substrates was observed comparing to the ZnO nanolayers grown by ALD on Si substrates. Significant enhancement of the band-edge emission of ZnO in Bi_2Se_3/ZnO heterostructures was observed. Three main mechanisms of the PL improvement are proposed: (i) decrease of the depletion layer due to the charge transfer at the Bi_2Se_3/ZnO interface and formation of the hole-rich and electron-rich zones in Bi_2Se_3 and ZnO respectively; (ii) improvement of the ZnO crystallinity, especially in the ZnO nanolayers in

G/Bi_2Se_3/ZnO heterostructures, and (iii) resonance of ZnO excitons with Bi_2Se_3 surface plasmon polaritons at the Bi_2Se_3/ZnO interface. Analysis of the defect PL revealed its dependence on the width of the depletion layer and the average grain size of the ZnO. Bi_2Se_3 and ZnO showed good compatibility of both Q/Bi_2Se_3/ZnO and G/Bi_2Se_3/ZnO heterostructures and their high potential for applications in optoelectronic devices.

ACKNOWLEDGEMENTS

This work was funded by the ERDF project No. 1.1.1.1/16/A/257, Taiwan–Latvia–Lithuania Cooperation Project LV–LT–TW/2019/1 and the European Union's Horizon 2020 research and innovation program under grant agreement No: 778157 – CanBioSe.

Work related to TEM studies was performed at the Center for Integrated Nanotechnologies, an Office of Science User Facility operated for the U.S. Department of Energy (DOE) Office of Science. Los Alamos National Laboratory, an affirmative action equal opportunity employer, is managed by Triad National Security, LLC for the U.S. Department of Energy's NNSA, under contract 89233218CNA000001.

CORRESPONDING AUTHOR.

*E-mail: donats.erts@lu.lv

REFERENCES.

(1) Özgür, Ü.; Alivov, Y. I.; Liu, C.; Teke, A.; Reshchikov, M. A.; Doğan, S.; Avrutin, V.; Cho, S. J.; Morkoç, H. A Comprehensive Review of ZnO Materials and Devices. *J. Appl. Phys.* **2005**, *98*, 041301.

(2) Son, D. I.; Kwon, B. W.; Park, D. H.; Seo, W. S.; Yi, Y.; Angadi, B.; Lee, C. L.; Choi, W. K.

Emissive ZnO-Graphene Quantum Dots for White-Light-Emitting Diodes. *Nat. Nanotechnol.* **2012**, *7*, 465–471.

(3) Liang, Y. C.; Zhao, Q.; Liu, K. K.; Liu, Q.; Lu, X. L.; Wu, X. Y.; Lu, Y. J.; Dong, L.; Shan, C. X. Ultrasensitive Mechano-Stimuli Luminescence Enhancement in ZnO Nanoparticles. *J. Phys. Chem. Lett.* **2019**, *10*, 3557–3562.

(4) Chaaya, A. A.; Bechelany, M.; Balme, S.; Miele, P. ZnO 1D Nanostructures Designed by Combining Atomic Layer Deposition and Electrospinning for UV Sensor Applications. *J. Mater. Chem. A* **2014**, *2*, 20650–20658.

(5) Ning, Y.; Zhang, Z.; Teng, F.; Fang, X. Novel Transparent and Self-Powered UV Photodetector Based on Crossed ZnO Nanofiber Array Homojunction. *Small* **2018**, *14*, 1703754.

(6) Zhao, B.; Wang, F.; Chen, H.; Zheng, L.; Su, L.; Zhao, D.; Fang, X. An Ultrahigh Responsivity (9.7 MA W^{-1}) Self-Powered Solar-Blind Photodetector Based on Individual ZnO–Ga_2O_3 Heterostructures. *Adv. Funct. Mater.* **2017**, *27*, 1700264.

(7) Zhang, Z.; Ning, Y.; Fang, X. From Nanofibers to Ordered ZnO/NiO Heterojunction Arrays for Self-Powered and Transparent UV Photodetectors. *J. Mater. Chem. C* **2019**, *7*, 223–229.

(8) Yuan, J.; Hu, L.; Xu, Z.; Zhang, Y.; Li, H.; Cao, X.; Liang, H.; Ruan, S.; Zeng, Y. J. Concurrent Improvement of Photocarrier Separation and Extraction in ZnO Nanocrystal Ultraviolet Photodetectors. *J. Phys. Chem. C* **2019**, *123*, 14766–14773.

(9) Ouyang, W.; Teng, F.; Jiang, M.; Fang, X. ZnO Film UV Photodetector with Enhanced Performance: Heterojunction with $CdMoO_4$ Microplates and the Hot Electron Injection Effect of Au Nanoparticles. *Small* **2017**, *13*, 1702177.

(10) Ahn, M. W.; Park, K. S.; Heo, J. H.; Kim, D. W.; Choi, K. J.; Park, J. G. On-Chip Fabrication of ZnO-Nanowire Gas Sensor with High Gas Sensitivity. *Sensors Actuators, B Chem.* **2009**, *138*, 168–173.

(11) Tamashevski, A.; Harmaza, Y.; Viter, R.; Jevdokimovs, D.; Poplausks, R.; Slobozhanina, E.; Mikoliunaite, L.; Erts, D.; Ramanaviciene, A.; Ramanavicius, A. Zinc Oxide Nanorod Based Immunosensing Platform for the Determination of Human Leukemic Cells. *Talanta* **2019**, *200*, 378–386.

(12) Viter, R.; Savchuk, M.; Starodub, N.; Balevicius, Z.; Tumenas, S.; Ramanaviciene, A.; Jevdokimovs, D.; Erts, D.; Iatsunskyi, I.; Ramanavicius, A. Photoluminescence Immunosensor Based on Bovine Leukemia Virus Proteins Immobilized on the ZnO Nanorods. *Sensors Actuators, B Chem.* **2019**, *285*, 601–606.

(13) Weber, M.; Julbe, A.; Ayral, A.; Miele, P.; Bechelany, M. Atomic Layer Deposition for Membranes: Basics, Challenges, and Opportunities. *Chem. Mater.* **2018**, *30*, 7368–7390.

(14) Chaaya, A. A.; Viter, R.; Baleviciute, I.; Bechelany, M.; Ramanavicius, A.; Gertnere, Z.; Erts, D.; Smyntyna, V.; Miele, P. Tuning Optical Properties of Al_2O_3/ZnO Nanolaminates Synthesized by Atomic Layer Deposition. *J. Phys. Chem. C* **2014**, *118*, 3811–3819.

(15) Viter, R.; Abou Chaaya, A.; Iatsunskyi, I.; Nowaczyk, G.; Kovalevskis, K.; Erts, D.; Miele, P.; Smyntyna, V.; Bechelany, M. Tuning of ZnO 1D Nanostructures by Atomic Layer Deposition and Electrospinning for Optical Gas Sensor Applications. *Nanotechnology* **2015**, *26*, 105501.

(16) Viter, R.; Iatsunskyi, I.; Fedorenko, V.; Tumenas, S.; Balevicius, Z.; Ramanavicius, A.; Balme, S.; Kempiński, M.; Nowaczyk, G.; Jurga, S.; et al. Enhancement of Electronic and Optical

Properties of ZnO/Al_2O_3 Nanolaminate Coated Electrospun Nanofibers. *J. Phys. Chem. C* **2016**, *120*, 5124–5132.

(17) Baitimirova, M.; Viter, R.; Andzane, J.; Van Der Lee, A.; Voiry, D.; Iatsunskyi, I.; Coy, E.; Mikoliunaite, L.; Tumenas, S.; Zaleski, K.; et al. Tuning of Structural and Optical Properties of Graphene/ZnO Nanolaminates. *J. Phys. Chem. C* **2016**, *120*, 23716–23725.

(18) Iatsunskyi, I.; Baitimirova, M.; Coy, E.; Yate, L.; Viter, R.; Ramanavicius, A.; Jurga, S.; Bechelany, M.; Erts, D. Influence of ZnO/Graphene Nanolaminate Periodicity on Their Structural and Mechanical Properties. *J. Mater. Sci. Technol.* **2018**, *34*, 1487–1493.

(19) Bera, S.; Ghosh, S.; Basu, R. N. Fabrication of Bi_2S_3/ZnO Heterostructures: An Excellent Photocatalyst for Visible-Light-Driven Hydrogen Generation and Photoelectrochemical Properties. *New J. Chem.* **2018**, *42*, 541–554.

(20) Xia, Y.; Qian, D.; Hsieh, D.; Wray, L.; Pal, A.; Lin, H.; Bansil, A.; Grauer, D.; Hor, Y. S.; Cava, R. J.; et al. Observation of a Large-Gap Topological-Insulator Class with a Single Dirac Cone on the Surface. *Nat. Phys.* **2009**, *5*, 398–402.

(21) Andzane, J.; Kunakova, G.; Charpentier, S.; Hrkac, V.; Kienle, L.; Baitimirova, M.; Bauch, T.; Lombardi, F.; Erts, D. Catalyst-Free Vapour-Solid Technique for Deposition of Bi_2Te_3 and Bi_2Se_3 Nanowires/Nanobelts with Topological Insulator Properties. *Nanoscale* **2015**, *7*, 15935–15944.

(22) Xiu, F.; He, L.; Wang, Y.; Cheng, L.; Chang, L. Te; Lang, M.; Huang, G.; Kou, X.; Zhou, Y.; Jiang, X.; et al. Manipulating Surface States in Topological Insulator Nanoribbons. *Nat. Nanotechnol.* **2011**, *6*, 216–221.

(23) Kunakova, G.; Galletti, L.; Charpentier, S.; Andzane, J.; Erts, D.; Léonard, F.; Spataru, C. D.;

Bauch, T.; Lombardi, F. Bulk-Free Topological Insulator Bi_2Se_3 Nanoribbons with Magnetotransport Signatures of Dirac Surface States. *Nanoscale* **2018**, *10*, 19595–19602.

(24) Liao, Z. M.; Han, B. H.; Wu, H. C.; Yashina, L. V.; Yan, Y.; Zhou, Y. B.; Bie, Y. Q.; Bozhko, S. I.; Fleischer, K.; Shvets, I. V.; et al. Surface Plasmon on Topological Insulator/Dielectric Interface Enhanced ZnO Ultraviolet Photoluminescence. *AIP Adv.* **2012**, *2*, 022105.

(25) Hong, S. S.; Cha, J. J.; Kong, D.; Cui, Y. Ultra-Low Carrier Concentration and Surface-Dominant Transport in Antimony-Doped Bi_2Se_3 Topological Insulator Nanoribbons. *Nat. Commun.* **2012**, *3,* 757.

(26) Baitimirova, M.; Andzane, J.; Petersons, G.; Meija, R.; Poplausks, R.; Romanova, M.; Erts, D. Vapor–Solid Synthesis and Enhanced Thermoelectric Properties of Non-Planar Bismuth Selenide Nanoplates on Graphene Substrate. *J. Mater. Sci.* **2016**, *51*, 8224–8232.

(27) Mattevi, C.; Kim, H.; Chhowalla, M. A Review of Chemical Vapour Deposition of Graphene on Copper. *J. Mater. Chem.* **2011**, *21*, 3324-3334.

(28) Ghoneim, M. T.; Smith, C. E.; Hussain, M. M. Simplistic Graphene Transfer Process and Its Impact on Contact Resistance. *Appl. Phys. Lett.* **2013**, *102*, 183115.

(29) Andzane, J.; Britala, L.; Kauranens, E.; Neciporenko, A.; Baitimirova, M.; Lara-Avila, S.; Kubatkin, S.; Bechelany, M.; Erts, D. Effect of Graphene Substrate Type on Formation of Bi_2Se_3 Nanoplates. *Sci. Rep.* **2019**, *9*, 4791.

(30) Andzane, J.; Buks, K.; Strakova, M. N.; Zubkins, M.; Bechelany, M.; Marnauza, M.; Baitimirova, M.; Erts, D. Structure and Doping Determined Thermoelectric Properties of Bi_2Se_3 Thin Films Deposited by Vapour-Solid Technique. *IEEE Trans. Nanotechnol.* **2019**, *18*, 948–954.

(31) Chaaya, A. A.; Viter, R.; Bechelany, M.; Alute, Z.; Erts, D.; Zalesskaya, A.; Kovalevskis, K.; Rouessac, V.; Smyntyna, V.; Miele, P. Evolution of Microstructure and Related Optical Properties of ZnO Grown by Atomic Layer Deposition. *Beilstein J. Nanotechnol.* **2013**, *4*, 690–698.

(32) Benchaabane, A.; Ben Hamed, Z.; Kouki, F.; Abderrahmane Sanhoury, M.; Zellama, K.; Zeinert, A.; Bouchriha, H. Performances of Effective Medium Model in Interpreting Optical Properties of Polyvinylcarbazole:ZnSe Nanocomposites. *J. Appl. Phys.* **2014**, *115*, 134313.

(33) Ding, Z.; Bux, S. K.; King, D. J.; Chang, F. L.; Chen, T. H.; Huang, S. C.; Kaner, R. B. Lithium Intercalation and Exfoliation of Layered Bismuth Selenide and Bismuth Telluride. *J. Mater. Chem.* **2009**, *19*, 2588–2592.

(34) Calestani, G. Introduction to Crystallography. *Adv. Imag. Elect. Phys.* **2002**, *123*, 29-70.

(35) Bindu, P.; Thomas, S. Estimation of Lattice Strain in ZnO Nanoparticles: X-Ray Peak Profile Analysis. *J. Theor. Appl. Phys.* **2014**, *8*, 123–134.

(36) R. Saleh, W.; M. Saeed, N.; A. Twej, W.; Alwan, M. Synthesis Sol-Gel Derived Highly Transparent ZnO Thin Films for Optoelectronic Applications. *Adv. Mater. Phys. Chem.* **2012**, *02*, 11–16.

(37) Liang, W. Y.; Yoffe, A. D. Transmission Spectra of ZnO Single Crystals. *Phys. Rev. Lett.* **1968**, *20*, 59–62.

(38) Arif, A.; Belahssen, O.; Gareh, S.; Benramache, S. The Calculation of Band Gap Energy in Zinc Oxide Films. *J. Semicond.* **2015**, *36*, 013001.

(39) Fang, J.; Fan, H.; Ma, Y.; Wang, Z.; Chang, Q. Surface Defects Control for ZnO Nanorods

Synthesized by Quenching and Their Anti-Recombination in Photocatalysis. *Appl. Surf. Sci.* **2015**, *332*, 47–54.

(40) Antony, A.; Poornesh, P.; Kityk, I. V.; Myronchuk, G.; Sanjeev, G.; Petwal, V. C.; Verma, V. P.; Dwivedi, J. A Study of 8 MeV E-Beam on Localized Defect States in ZnO Nanostructures and Its Role on Photoluminescence and Third Harmonic Generation. *J. Lumin.* **2019**, *207*, 321–332.

(41) Janotti, A.; Van De Walle, C. G. Fundamentals of Zinc Oxide as a Semiconductor. *Reports Prog. Phys.* **2009**, *72*, 126501.

(42) Janotti, A.; Van De Walle, C. G. Native Point Defects in ZnO. *Phys. Rev. B* **2007**, *76*, 165202.

(43) Edmonds, M. T.; Hellerstedt, J. T.; Tadich, A.; Schenk, A.; Donnell, K. M. O.; Tosado, J.; Butch, N. P.; Syers, P.; Paglione, J.; Fuhrer, M. S. Stability and Surface Reconstruction of Topological Insulator Bi_2Se_3 on Exposure to Atmosphere. *J. Phys. Chem. C* **2014**, *118*, 20413-20419.

(44) Edmonds, M. T.; Hellerstedt, J. T.; Tadich, A.; Schenk, A.; O'Donnell, K. M.; Tosado, J.; Butch, N. P.; Syers, P.; Paglione, J.; Fuhrer, M. S. Air-Stable Electron Depletion of Bi_2Se_3 Using Molybdenum Trioxide into the Topological Regime. *ACS Nano* **2014**, *8*, 6400–6406.

(45) Spataru, C. D.; Léonard, F. Fermi-Level Pinning, Charge Transfer, and Relaxation of Spin-Momentum Locking at Metal Contacts to Topological Insulators. *Phys. Rev. B* **2014**, *90*, 085115.

(46) Reshchikov, M. A.; Behrends, A.; Bakin, A.; Waag, A. Photoluminescence from ZnO Nanowires. *J. Vac. Sci. Technol. B Microelectron. Nanom. Struct.* **2009**, *27*, 1688.

TOC figure.

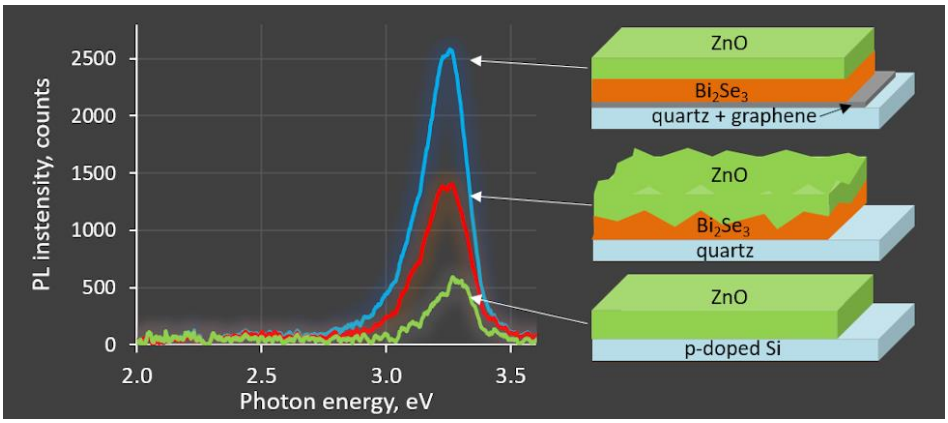
PL instensity, counts
2500
2000
1500
1000
500
0
2.0
2.5
3.0
3.5
Photon energy, eV
ZnO
Bi2Se3
quartz + graphene
ZnO
Bi2Se3
quartz
ZnO
p-doped Si